Eliminating the Low-Frequency Breakdown Problem in 3-D Full-Wave Finite-Element-Based Analysis of Integrated Circuits

Jianfang Zhu, *Student Member, IEEE*, and Dan Jiao, *Senior Member, IEEE*

***Abstract*—An effective method is developed in this work to extend the validity of a full-wave finite-element-based solution down to dc for general 3-D problems. In this method, we accurately decompose the Maxwell's system at low frequencies into two subsystems in the framework of a full-wave-based solution. One has an analytical frequency dependence, whereas the other can be solved at frequencies as low as dc. Thus, we bypass the numerical difficulty of solving a highly ill-conditioned and even singular system at low frequencies. In addition, we provide a theoretical analysis on the conditioning of the matrices of the original coupled Maxwell's system and the decomposed system. We show that the decomposed system is well conditioned, and also positive definite at dc. The validity and accuracy of the proposed method have been demonstrated by extraction of state-of-the-art on-chip integrated circuits at frequencies as low as dc.**

The proposed method bypasses the need for switching basis functions. Furthermore, it avoids stitching static- and full-wave-based solvers. The same system matrix is used across all the frequencies from high to low frequencies. Hence, the proposed method can be incorporated into any existing full-wave finite-element-based computer-aided design tool with great ease to completely remove the low-frequency breakdown problem.

***Index Terms*—Electromagnetic analysis, finite-element methods (FEMs), full-wave analysis, integrated circuits (ICs), low-frequency breakdown.**

I. Introduction

THERE EXISTS a wide range of applications in which frequencies ranging from dc to high frequencies are involved. For example, the design of high-speed digital, analog, mixed-signal, and RF integrated circuits (ICs) from dc to tens and hundreds of gigahertz frequencies. In such a broad band of frequencies, static-based modeling and simulation tools have fundamental limits in capturing high-frequency effects accurately. In contrast, full-wave-based modeling and simulation tools can capture high-frequency effects accurately. However, they generally break down at low frequencies [1]–[10]. In order to perform circuit design in a broad band of frequencies, a natural solution is to stitch a static-based computer-aided design (CAD) tool with a full-wave-based CAD tool. However, this solution is cumbersome because one has to develop and accommodate both tools and switch between these two when necessary. The other popular solution is to change basis functions. For example, the loop-tree and loop-star basis functions [1], [7] were used to achieve a natural Helmholtz decomposition of the current to overcome the low-frequency breakdown problem in integral-equation-based methods. As another example, the tree–cotree splitting scheme [4], [5] was used to provide an approximate Helmholtz decomposition for edge elements in finite-element-based methods. The edge basis functions were used on the cotree edges, whereas the scalar basis functions were incorporated on the free nodes associated with the tree edges to represent the gradient field. Again, this solution is not convenient since one has to change basis functions to extend the applicability of a full-wave solver to low frequencies.

More important, existing tree–cotree splitting based solutions of vector wave equations cannot be used to fundamentally solve the low-frequency breakdown problem. We will soon establish in the sequel that the system matrix resulting from the tree–cotree splitting for solving vector wave equations remains singular at low frequencies, although the tree–cotree splitting scheme was successful in eliminating the null space of the curl operator in magnetostatic analysis [13]. As yet, no results have been reported at frequencies as low as dc for on-chip applications in which the physical dimensions could be less than 1 μm. For example, it was shown that a tree–cotree splitting scheme can be used to extend a full-wave finite-element method (FEM)-based solution to 1 MHz for typical on-chip dimensions [5]. However, for frequencies lower than 1 MHz, extrapolation techniques are required.

In this work, we consider the following two questions. 1) Whether we switch basis functions or we switch solvers, the system matrix has to be reformulated. The resultant computational overhead is nontrivial. Can we extend the validity of a full-wave FEM-based solver to low frequencies without changing the system matrix? If this can be done, we can, with great ease, fix the low-frequency breakdown problem in existing full-wave FEM-based CAD tools. 2) Can we extend the validity of a full-wave FEM-based solver to frequencies as low as dc? In other words, can we completely eliminate the low-frequency breakdown problem? The answers to these two questions not only can be used to fundamentally overcome the

Manuscript received September 19, 2009; revised June 09, 2010; accepted June 28, 2010. Date of publication September 16, 2010; date of current version October 13, 2010. This work was supported by the Intel Corporation under a grant, the National Science Foundation (NSF) under NSF Grant 0747578, and by the Office of Naval Research under Grant N00014-10-1-0482.

The authors are with the School of Electrical and Computer Engineering, Purdue University, West Lafayette, IN 47907 USA (e-mail: zhu3@purdue.edu; djiao@purdue.edu).

Color versions of one or more of the figures in this paper are available online at http://ieeexplore.ieee.org.

Digital Object Identifier 10.1109/TMTT.2010.2065930

low-frequency breakdown problem, but also can be used to develop unconditionally stable time-domain numerical schemes because the use of a large time step suggests that frequencies to be solved are low.

In [10], we developed an FEM-based solution that addressed both questions in the framework of a 2.5-D eigenvalue-based FEM method for the broadband modeling of on-chip interconnects. In this paper, we propose an effective solution to eliminate the low-frequency breakdown problem in a 3-D FEM-based solution of vector wave equations. This solution addresses the two questions raised above. It uses the same system matrix across all frequencies. Meanwhile, it is valid at frequencies as low as dc. In addition, we provide a theoretical analysis on the root cause of the low-frequency breakdown problem observed in the solution of vector wave equations, and the reason why this problem is extremely severe in the modeling of very large scale integrated (VLSI) circuits. We show that existing tree–cotree splitting based solutions cannot be used to completely solve the low-frequency breakdown problem for vector wave equations. In addition, a pure mathematics-based matrix scaling technique cannot be used to remove the low-frequency breakdown problem either because physics dictates that the eigenvalue spectrum present in a full-wave FEM-based analysis of ICs is ultra large. We thus develop a method that can bypass the numerical difficulty of solving a highly ill-conditioned system. This method is developed by decomposing the Maxwell's coupled system into two subsystems at low frequencies in the framework of a full-wave based solution. One system has an analytical frequency dependence, while the other has a well-conditioned matrix down to dc. In addition, the existence of the dc solution in the proposed method is also proved. Our proposed approach constitutes a unified finite-element solution because across all the frequencies, we use the same system matrix. With that, we are able to incorporate the proposed solution into any existing FEM solver to remove the low-frequency problem with great ease.

II. Low-Frequency Breakdown Problem

A. 3-D Full-Wave Finite-Element-Based Solution

Consider the second-order vector wave equation subject to a certain boundary condition

$$\nabla \times \left[\mu_r^{-1} \nabla \times \mathbf{E}\right] - \omega^2 \epsilon_r / c^2 \mathbf{E} + j\omega\mu_0\sigma\mathbf{E} = -j\omega\mu_0\mathbf{J} \quad (1)$$

where μ_r is relative permeability, ϵ_r is relative permittivity, σ is conductivity, ω is angular frequency, c is the speed of light, and $\mathbf{J}$ represents a current source. When discretizing (1), the conducting region in the computational domain is also discretized in order to model fields inside conductors accurately. This is especially important at low frequencies because conductors become transparent to fields due to large skin depth.

By expanding the unknown $\mathbf{E}$ using vector basis function $\mathbf{N}$ as

$$\mathbf{E} = \sum_{i=1}^{n} u_i \mathbf{N}_i \quad (2)$$

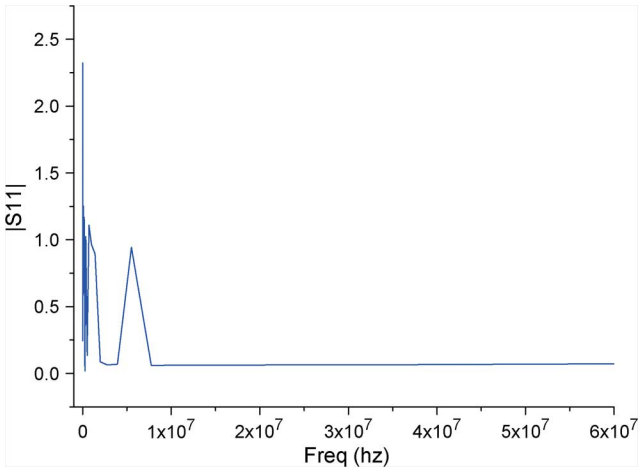

Fig. 1. Low-frequency breakdown observed in the modeling of on-chip circuits.

a finite-element-based analysis of (1) yields the following matrix equation

$$\mathbf{K}u = b. \quad (3)$$

If the first-order absorbing boundary condition is used to truncate the computational domain, $\mathbf{K}$ and b are assembled from their elemental counterparts as

$$\begin{aligned}\mathbf{K}^e = &\mu_r^{-1} \iiint_V (\nabla \times \mathbf{N}_i \cdot \nabla \times \mathbf{N}_j) dV \\ &- \omega^2 \epsilon_r / c^2 \iiint_V (\mathbf{N}_i \cdot \mathbf{N}_j) dV \\ &+ j\omega\mu_0\sigma \iiint_V (\mathbf{N}_i \cdot \mathbf{N}_j) dV, \\ &+ j\omega/c \iint_{S_0} (\hat{n} \times \mathbf{N}_i \cdot \hat{n} \times \mathbf{N}_j) dS \\ b^e = &- j\omega\mu_0 \iiint_V (\mathbf{N}_i \cdot \mathbf{J}) dV. \end{aligned} \quad (4)$$

In a full-wave analysis, a commonly used vector basis function is edge element [11]. We used edge basis functions in a triangular prism element for all the simulations conducted in this work.

It was shown by our numerical experiments that, in general, the solution of (3) breaks down at tens of megahertz in typical on-chip problems, the electric size of which can be smaller than 10^{-9} wavelengths. As an example, consider a short single wire of 1-μm dimension embedded in an inhomogeneous stack. The magnitude of reflection coefficient S_{11} is theoretically predicted to be very close to zero at low frequencies. However, as can be seen from Fig. 1, S_{11} obtained from an FEM solution is wrong at low frequencies. In this example, the conductor loss inside the conducting wire is significant. As another example, which is lossless, consider a 1 μm $\times$ 1 μm $\times$ 1 μm parallel-plate structure made of perfect conductors. In Fig. 2(a), we plot the analytical solution of $\mathbf{E}$'s magnitude at each edge in the computational domain at 10 kHz. In Fig. 2(b), we plot $\mathbf{E}$'s magnitude at each

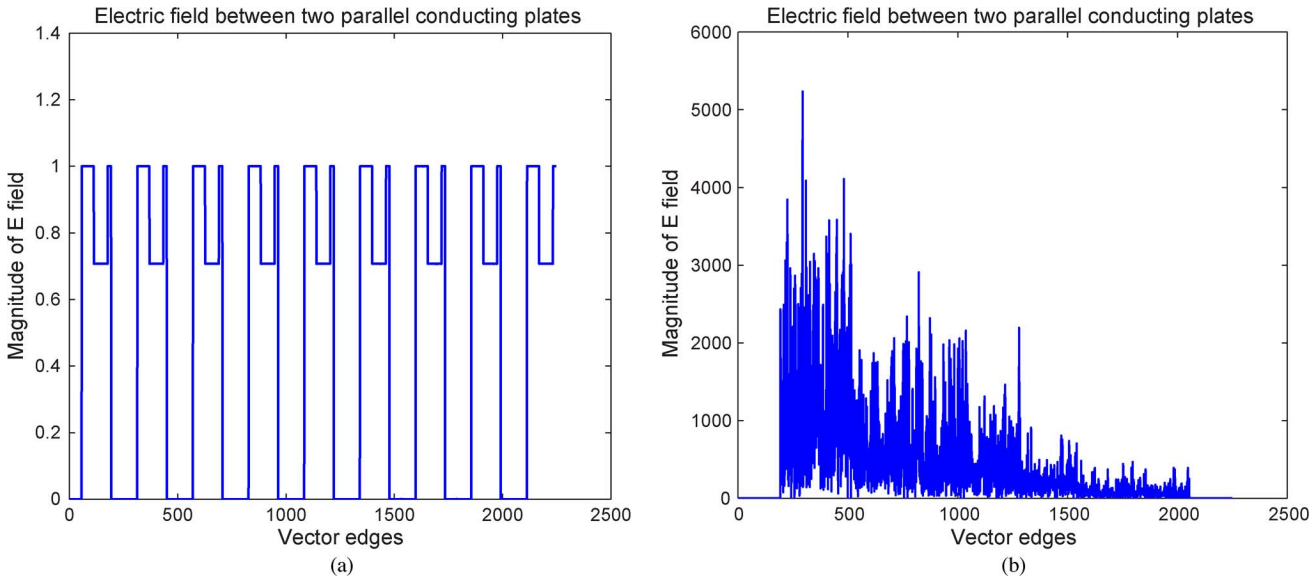

Fig. 2. Magnitude of the electric field between two parallel plates made of perfect conductors. (a) Analytical result. (b) Numerical result, which breaks down.

edge obtained by numerically solving (3) at 10 kHz. Clearly, the FEM solution breaks down. The low-frequency breakdown problem is analyzed in Section II-B.

B. Analysis of Low-Frequency Breakdown Problem

Matrix $\mathbf{K}$ in (3) can be written as

$$\mathbf{K} = \mathbf{S} - \omega^2\mathbf{T} + j\omega\mathbf{R} \tag{5}$$

where

$$\begin{aligned}\mathbf{S} &= \mu_r^{-1}\iiint_V (\nabla\times\mathbf{N}_i\cdot\nabla\times\mathbf{N}_j)dV\\ \mathbf{T} &= \epsilon_r/c^2\iiint_V (\mathbf{N}_i\cdot\mathbf{N}_j)dV\\ \mathbf{R} &= \mu_0\sigma\iiint_V (\mathbf{N}_i\cdot\mathbf{N}_j)dV\\ &\quad + 1/c\iint_{S_0}(\hat{n}\times\mathbf{N}_i\cdot\hat{n}\times\mathbf{N}_j)dS.\end{aligned} \tag{6}$$

1) On the Conditioning of the System Matrix: To understand the low-frequency breakdown problem, we first consider a lossless system

$$\mathbf{K} = \mathbf{S} - \omega^2\mathbf{T}. \tag{7}$$

The eigenvalue distribution of (7) can be analyzed via the following generalized eigenvalue problem

$$\mathbf{S}x = \lambda\mathbf{T}x. \tag{8}$$

Since $\mathbf{S}$ is symmetric semipositive definite and $\mathbf{T}$ is symmetric positive definite, the eigenvalues of (8) are nonnegative real numbers. They are located on the real axis, as shown in Fig. 3(a). Among these eigenvalues, some are zero because of the null space of $\mathbf{S}$ [3]. The remaining eigenvalues correspond to the resonant frequencies of the 3-D structure being simulated. For IC problems, except for the eigenvalues associated with the dominant gradient-type modes, these eigenvalues are extremely large because the geometrical dimensions of on-chip circuits are very small.

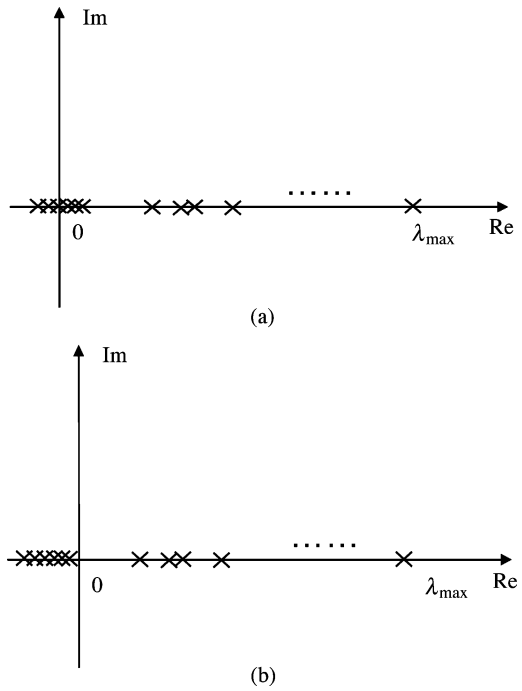

Fig. 3. Illustration of the eigenvalue distribution. (a) Eigenvalues of (8). (b) Eigenvalue distribution related to $\mathbf{S} - \omega^2\mathbf{T}$.

Denoting the eigenvalues of (8) by $\lambda_1, \lambda_2 \ldots \lambda_N$, and the corresponding eigenvectors by $x_1, x_2, \ldots, x_N$, let $\Phi = [x_1, x_2, \ldots, x_N]$. Since Φ are $\mathbf{T}$ orthogonal, we obtain

$$\phi^T(\mathbf{S} - \omega^2\mathbf{T})\phi = \begin{pmatrix}\lambda_1 - \omega^2 & \cdots & 0\\ \vdots & \ddots & \vdots\\ 0 & \cdots & \lambda_N - \omega^2\end{pmatrix} \tag{9}$$

which can be used to analyze the condition number of (7).

From (9), it can be seen that the eigenspace of (8) is shifted to the left by ω^2, as illustrated in Fig. 3(b). All the zero eigenvalues are shifted to the left plane, while the nonzero ones remain in the right plane since the ω considered here are small, denoting the maximum eigenvalue of (8) by $\lambda_{\max}$. The condition number of (9) is

$$\frac{\lambda_{\max}-\omega^2}{\omega^2} \tag{10}$$

which is very large since $\lambda_{\max}$ is tens of orders of magnitude larger than ω^2. Take a typical IC structure for example, the condition number can be as large as 10^{25} at 1 Hz. Moreover, as the frequency decreases, the condition number increases. As a result, the full-wave-based system (7) becomes highly ill conditioned at low frequencies. At dc, the system even becomes singular.

In addition, because of numerical errors, the eigenvalues of (8) due to the null space of $\mathbf{S}$ are not exactly zeros. Instead, they are clustered around the origin point in the complex plane. The same is true for gradient-type modes that are physical. This problem may not even exist in microwave or millimeter-wave circuits. However, it is very severe in on-chip VLSI circuits because the eigenvalues of (8) spread over a much wider spectrum compared to those in microwave or millimeter-wave circuits. Thus, the eigenvalues, which theoretically should be zero, cannot be obtained as zero numerically. In fact, our numerical experiments show significant values. This is understandable because computers have finite precision. If there exists an eigenvalue that is as large as 10^{25}, it is very difficult to find zero eigenvalues correctly. When frequency is high, the inexact zero eigenvalues do not induce much error because $\lambda-\omega^2$ is still approximately equal to $-\omega^2$ even if λ is not exactly zero. However, at low frequencies, the error can be very significant. The value of $-\omega^2$ can even be overwhelmed by the inaccurate λ when ω is small. As a result, the frequency dependence of the electric field extracted out of (7) can be wrong at low frequencies. Moreover, if ω^2 hits one of the inexact eigenvalues clustered around the origin point, the system can even become singular. The low-frequency breakdown problem observed in a lossy system shown in (5) can also be understood by a similar analysis.

2) On the Tree–Cotree Splitting Based Solutions of Vector Wave Equations: The tree–cotree splitting has been used to solve the low-frequency breakdown problem in a finite-element-based solution of vector wave equations. However, in the following, we show that existing techniques based on tree–cotree splitting cannot be used to completely solve the low-frequency breakdown problem, although it has been used to successfully eliminate the null space of the curl operator for magnetostatic applications [13].

Consider a magnetostatic problem

$$\nabla\times\left[\mu_r^{-1}\nabla\times\mathbf{A}\right]=\mathbf{J} \tag{11}$$

a finite-element-based analysis of (11) results in the following matrix system:

$$\begin{pmatrix}\mathbf{S}_{CC} & \mathbf{S}_{CT}\\ \mathbf{S}_{TC} & \mathbf{S}_{TT}\end{pmatrix}\begin{pmatrix}\mathbf{A}_C\\ \mathbf{A}_T\end{pmatrix}=\begin{pmatrix}b_C\\ b_T\end{pmatrix} \tag{12}$$

where subscripts C and T denote the quantities associated with a cotree and tree, respectively, and $\mathbf{S}$ is the same as shown in (6). It has been shown that the null space of $\mathbf{S}$ is related to the tree edges in a mesh. By arbitrarily setting the value of A_T on the tree edges, (12) is reduced to the following system:

$$\mathbf{S}_{CC}A_C=b_C-\mathbf{S}_{CT}A_T \tag{13}$$

where $\mathbf{S}_{CC}$ is symmetric positive definite. Therefore, for magnetostatic problems, the tree–cotree splitting successfully converts a singular matrix to a matrix that is solvable.

In existing solutions of vector wave equations based on tree–cotree splitting, the edge basis functions are used on the cotree edges. In addition, the scalar basis functions are used on the free nodes associated with tree edges to represent the gradient field. The resultant system matrix is

$$\begin{pmatrix}\mathbf{S}_{CC}-\omega^2\mathbf{T}_{CC}+j\omega\mathbf{R}_{CC} & -\omega^2\mathbf{T}_{1,CT}+j\omega\mathbf{R}_{1,CT}\\ -\omega^2\mathbf{T}_{1,TC}+j\omega\mathbf{R}_{1,TC} & -\omega^2\mathbf{T}_{2,TT}+j\omega\mathbf{R}_{2,TT}\end{pmatrix} \tag{14}$$

where $\mathbf{S}$, $\mathbf{T}$, and $\mathbf{R}$ are the same as those in (6), $\mathbf{T}_1$, $\mathbf{T}_2$, $\mathbf{R}_1$, and $\mathbf{R}_2$ are different because the gradient basis function is employed on the free nodes. Similar to the magnetostatic case, the sub-matrix $\mathbf{S}_{CC}$ is invertible. However, different from the magnetostatic case, the system cannot be reduced to a smaller one that only includes the CC part. Moreover, when frequency is close to zero, only the term involving the curl operator is left while all the other terms vanish because they are all frequency dependent. As a result, even though the tree–cotree gauge is introduced to eliminate the null space of a curl operator, the null space still exists in the TT portion of the matrix at low frequencies. In addition, different from that in magnetostatic cases, the upper left block of the system shown in (14) is now a combination of $\mathbf{S}$, $\mathbf{T}$, and $\mathbf{R}$ matrices. Although it will not become ill conditioned at low frequencies because $\mathbf{S}_{CC}$ is solvable now, the computed frequency dependence is, in fact, wrong due to the ignorance of the frequency dependent terms resulting from finite machine precision. Therefore, current tree–cotree splitting based methods have not fundamentally solved the low-frequency breakdown problem for vector wave equations.

Moreover, the mathematics-based matrix-condition-improving techniques cannot be used to fundamentally solve the low-frequency breakdown problem either. This is because the large spectrum of (8) is due to physical reasons instead of numerical reasons. The physical resonant modes of an IC structure determine the largest eigenvalue of the FEM system, which is very large because of the μm- and nm-level geometrical dimensions of an on-chip circuit, whereas the null space of $\mathbf{S}$ or the physical gradient field determines the smallest one, which is theoretically zero. As an example, we employed one of the most advanced scaling techniques [12] and found that it can only extend the full-wave-based solution to a frequency around 1 MHz.

In the following, we show an approach that can efficiently and effectively bypass the difficulty of solving an ill-conditioned system at low frequencies. Meanwhile, this approach can make the traditional full-wave FEM-based solution applicable to dc. Applications to on-chip problems of 1-μm dimensions have shown a success at frequencies as low as 0 Hz.

III. Proposed Method for Eliminating the Low-Frequency Breakdown Problem

We first elaborate a solution for problems that do not involve conductor loss, i.e., problems in which conductors are treated as perfect electric conductors. We then show how to handle problems that involve conductor loss, i.e., problems in which fields penetrate into conductors. In fact, when frequency is low, we have to consider the nonideality of conductors because the skin depth can be larger than the conductor dimension. As observed in on-chip VLSI circuits, conductors are transparent to fields. In this section, we also give a detailed analysis on the conditioning of the system matrix resulting from the proposed method.

A. Cases Without Conductor Loss

When there is no conductor loss, there is no $\mathbf{R}$ in (5). We consider a system shown in (7). At low frequencies where a full-wave solution breaks down, static solvers have been shown to produce accurate results. This suggests that at these frequencies, $\mathbf{E}$ and $\mathbf{H}$, are very well decoupled. Hence, for a problem that only involves perfect conductors, given a current source excitation $\mathbf{J}$ (the most commonly used excitation in an FEM-based analysis of circuits), the $\mathbf{E}$ field satisfies the following two equations:

$$\begin{aligned} \nabla \times \mathbf{E} &= 0 \\ \nabla \cdot \mathbf{D} &= -\frac{\nabla \cdot \mathbf{J}}{j\omega}. \end{aligned} \tag{15}$$

From (15), it is clear that $\mathbf{E}$ should scale with frequency as $O(\omega^{-1})$ given a constant current source excitation. The voltage thereby should scale with frequency as $O(\omega^{-1})$. The resultant voltage–current relationship suggests that a lossless low-frequency system that has perfect conductors is an effective capacitor, the capacitance of which does not change with frequency. At dc, the entire system that is external to the perfect conductor becomes an open circuit.

With the frequency dependence of the field solution analytically derived, we bypass the need for solving a highly ill-conditioned system (7) at low frequencies. Thus, the low-frequency breakdown problem can be readily overcome without the need of any computation. The procedure is as follows. Once the full-wave solution breaks down, we record the field solution u at the frequency that is a little bit higher than the breakdown frequency. It is clear that u is still valid at this frequency. We call this frequency the reference frequency. Denoting it by $\omega_{\rm ref}$ and the corresponding u by $u_{\rm ref}$, we can accurately obtain u at any lower frequency ω_L by using the following scaling:

$$u(\omega_L) = \omega_{\rm ref} \times u_{\rm ref}/\omega_L. \tag{16}$$

By doing so, we are able to accurately obtain the solution of the full-wave FEM-based system at low frequencies without switching basis functions or switching to static formulations.

B. Cases With Conductor Loss

The frequency dependence of the electric field in a lossless system has an analytical expression. To take advantage of that, for cases with conductor loss, we order unknowns inside conductors and those outside separately, yielding a system matrix as follows:

$$\begin{pmatrix} \mathbf{K}_{ii} & \mathbf{K}_{io} \\ \mathbf{K}_{oi} & \mathbf{K}_{oo} \end{pmatrix} \begin{pmatrix} u_i \\ u_o \end{pmatrix} = \begin{pmatrix} 0 \\ b_o \end{pmatrix} \tag{17}$$

where u_i denotes field unknowns inside conductors, u_o denotes those outside conductors; and b_o is the excitation placed outside conductors. Here, the excitation of b_i is not considered because in a full-wave FEM-based analysis of circuits, a current source excitation is generally launched from the ground to the port that is excited, and hence, excitation only exists in b_o. It is clear that $\mathbf{K}_{oo}$ in (17) is a lossless system.

Equation (17) constitutes a rigorous discretization of coupled Maxwell's equations. At low frequencies where a full-wave solution breaks down, $\mathbf{E}$ and $\mathbf{H}$ are very well decoupled. Therefore, in (17), if we set conduction current to be zero, we can solve for $\mathbf{E}$ only because the source for $\mathbf{H}$, which is the conduction current, is set to zero. If we do not enforce the condition that the conduction current is zero, we can solve for $\mathbf{H}$. The final solution of (17) can then be obtained by combining $\mathbf{E}$ and $\mathbf{H}$.

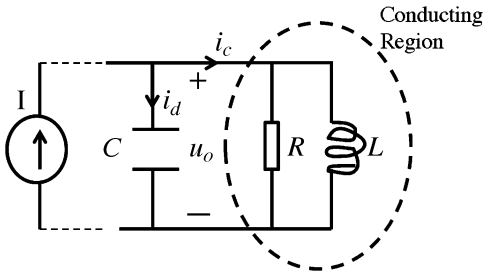

Fig. 4. Circuit representation of an FEM system shown in (5).

For clarity, we use a circuit interpretation of (5) to present the proposed solution of (17) at low frequencies. The FEM-based system (5) can be directly mapped to a circuit shown in Fig. 4. The second-order term related to frequency in (5) is associated with capacitance C, the first-order term is associated with resistance R, whereas the constant term is associated with inductance L. In Fig. 4, i_c denotes the conduction current, which can be evaluated from u_i in (17), whereas i_d denotes the displacement current.

In general, the effective R, L, and C shown in the figure are frequency dependent. However, at low frequencies, C is frequency independent. The proof is given below. From Fig. 4, C can be obtained from the resultant voltage–current relationship by setting the conduction current i_c to be zero. Since the conduction current density is σu_i, when the conduction current is zero, the u_i over the conducting region is also zero, and hence, the dielectric region is subject to an equivalent perfect electric conductor boundary condition. In such a lossless system, based on the analysis given in Section III-A, at low frequencies, since $\mathbf{E}$ and $\mathbf{H}$ are decoupled, given a constant current, the electric field, and hence, the voltage should scale with frequency as $O(\omega^{-1})$, as can be seen from (15). The resultant voltage–current relationship dictates a capacitance that does not change with frequency.

As a result, by setting conduction current u_i in (17) to be zero, we can solve for u_o given a current, from which the dielectric region external to the conductors, i.e., the C network, can be char-

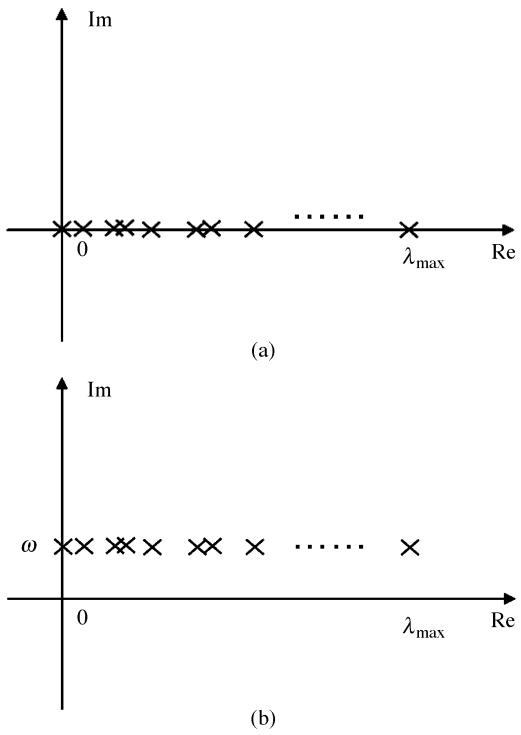

Fig. 5. Illustration of the eigenvalue distribution of the system matrix inside conductors. (a) Eigenvalue distribution of (21). (b) Up-shifted spectrum of (20).

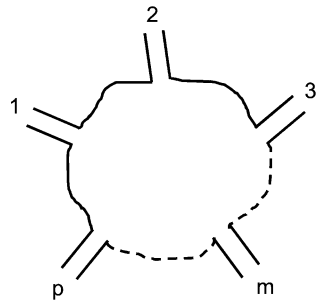

Fig. 6. Arbitrary N-port system.

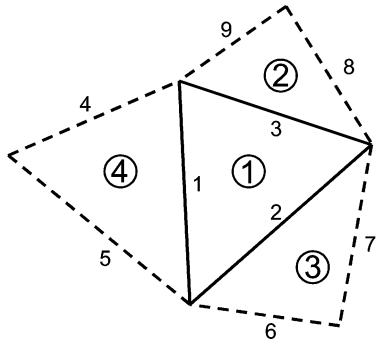

Fig. 7. Mesh with element 1 in the conducting region, and the other three elements in the dielectric region.

acterized. This characterization can be done at one frequency and used throughout the low-frequency range since C has no frequency dependence. The detail is given in Section III-B.1.

On the other hand, if we supply a voltage to the RL network, we can solve for u_i, from which the conducting region, i.e., the RL network, can be characterized. Note that different from C, RL are, in general, frequency dependent due to skin effects. Hence, u_i needs to be numerically solved at each frequency. The detail of this step is given in the following Section III-B.2.

After u_o subject to $u_i = 0$ is solved, and the u_i subject to a voltage source excitation is solved, we can combine the resultant u_o and u_i to obtain the S-parameters of the entire circuit, the detail of which is described in Section III-B.3.

From the aforementioned analysis, it can be seen that the coupled Maxwell's system involving conductor loss can be decomposed into two subsystems at low frequencies. One is the system outside conductors subject to perfect electric conducting boundary condition. This system has an analytical frequency dependence based on the analysis given in Section III-A. The other is the system inside conductors, which is $\mathbf{K}_{ii}$ in (17). We will show that this system is well conditioned even at dc in this section and Section III-C. Thus, we bypass the numerical difficulty of solving the highly ill-conditioned and even singular system (5) at low frequencies.

1) Solving for u_o Subject to $u_i = 0$: To characterize the system external to conductors, we set conduction current to be zero, and hence, $u_i = 0$. This is because the conduction current density is nothing but σu_i. As a result, (17) is reduced to

$$\mathbf{K}_{oo} u_o = b_o. \tag{18}$$

Clearly, it is a lossless system. The solution we have developed in Section III-A to solve the low-frequency breakdown problem for lossless cases can be directly used here to solve (18) at any low frequency. If the circuit parameter instead of u_o is of interest, once the full-wave solution breaks down, we record the field solution u at the frequency that is a little bit higher than the breakdown frequency, i.e., $\omega_{\rm ref}$, and use the capacitance extracted therein throughout the frequencies lower than $\omega_{\rm ref}$.

2) Solving for u_i: u_i is solved from the first equation in (17)

$$\mathbf{K}_{ii} u_i = -\mathbf{K}_{io} \tilde{u}_o \tag{19}$$

where $\tilde{u}_o$ serves as a voltage to excite the current inside conductors. Based on the analysis given in [17], such a voltage source excitation can be modeled as a gradient field. A natural and convenient choice of $\tilde{u}_o$ is $\mathrm{Re}[u_{o,\rm ref}]$, i.e., the real part of u_o solved from (17) at the reference frequency $\omega_{\rm ref}$. Since at $\omega_{\rm ref}$ and high frequencies current sources are generally used to perform a full-wave FEM-based analysis, the $\mathrm{Re}[u_{o,\rm ref}]$ is nothing but a voltage distribution over the resistance network of the conductors. Hence, it is a gradient field that serves as an effective excitation of (19).

Equation (19) can be solved at any low frequency because $\mathbf{K}_{ii}$ is a well-conditioned matrix. The proof is given as follows.

Since $\mathbf{K}_{ii}$ is formed inside conductors, it has the following form:

$$\mathbf{K}_{ii} = \mathbf{S}_{ii} + j\omega \mathbf{R}_{ii}. \tag{20}$$

The term associated with $\mathbf{T}$ is absent because inside conductors, the displacement current can be ignored compared to conduction current.

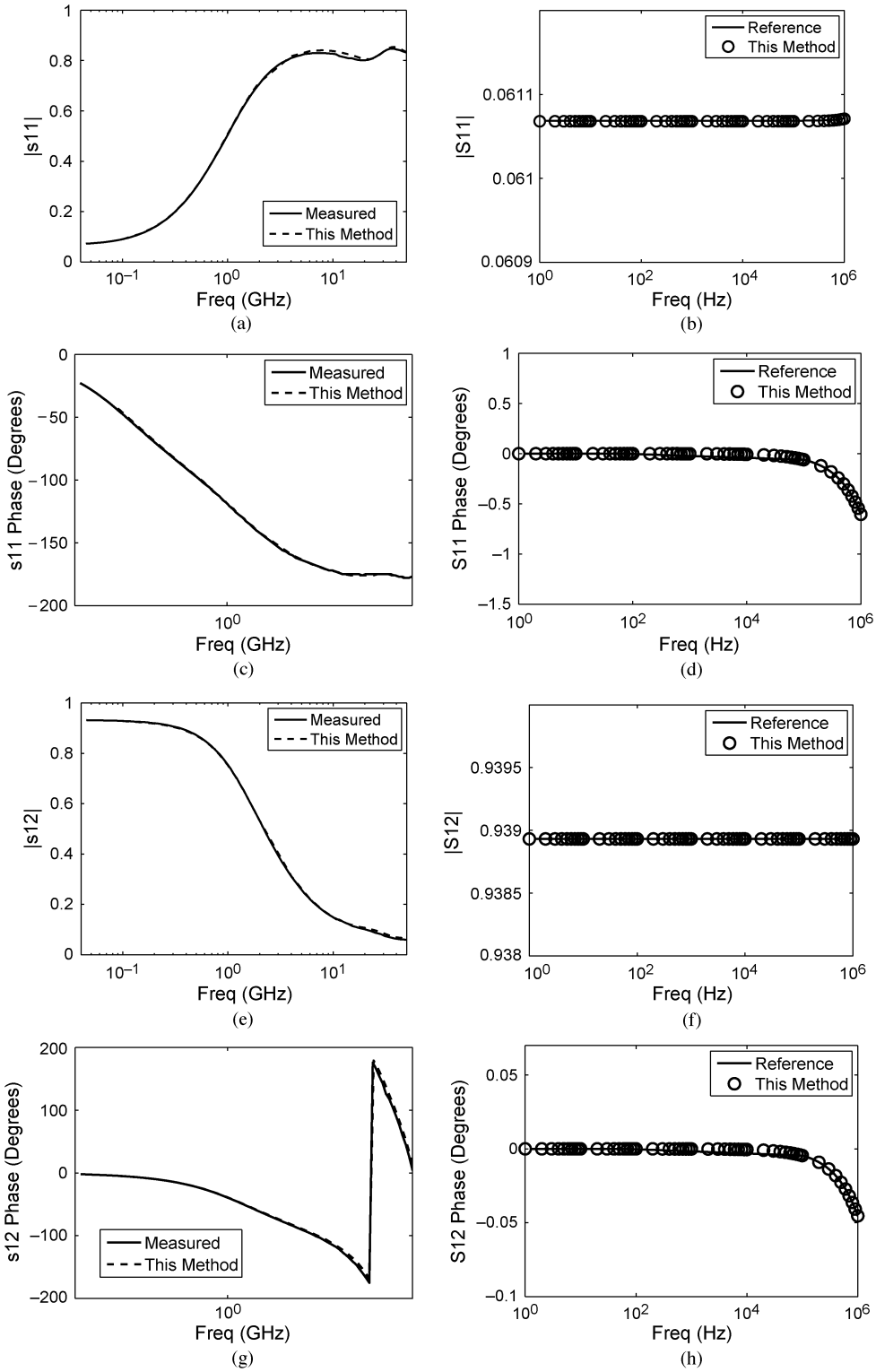

Fig. 8. S-parameters of an on-chip interconnect structure simulated by the proposed solution. (Left column: S-parameters in the entire band (frequency unit: gigahertz); right column: S-parameters at low frequencies (frequency unit: hertz).)

The eigenvalue distribution of (20) can be analyzed by considering the following eigenvalue problem:

$$\mathbf{S}_{ii}\tilde{x} = \tilde{\lambda}\mathbf{R}_{ii}\tilde{x}. \tag{21}$$

Since $\mathbf{R}_{ii}$ is symmetric positive definite and $\mathbf{S}_{ii}$ is at least semi-positive definite ($\mathbf{S}_{ii}$ can be made positive definite in the proposed solution, which is to be elaborated upon in Section III-C), the eigenvalues of (21) are nonnegative, as shown in Fig. 5(a). Similar to the analysis given in (9), when considering the system of $\mathbf{S}_{ii} + j\omega\mathbf{R}_{ii}$, we superpose $\tilde{\lambda}$ by $j\omega$. Therefore, the eigen-

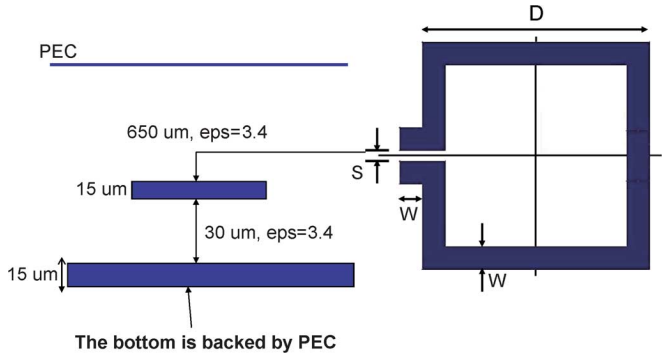

Fig. 9. Geometry of a 3-D spiral inductor (the perfect electric conductor is denoted as PEC).

values $\tilde{\lambda}$ are shifted upward by ω, as shown in Fig. 5(b). As can be seen, only a small shift in Fig. 5 can move the origin out of the eigenspace of $\mathbf{S}_{ii} + j\omega\mathbf{R}_{ii}$. In addition, the spectrum radius of (21) is approximately 10^{-20} smaller than that of (7) for good conductors because $\mathbf{R}$ is proportional to conductivity σ, whereas $\mathbf{T}$ is proportional to permittivity ϵ. For typical on-chip problems, the spectrum radius shown in Fig. 5 can be as small as 10^5. Hence, the matrix $\mathbf{K}_{ii}$ can be solved at low frequencies. In addition, in the proposed solution, $\mathbf{S}_{ii}$ can be made positive definite, and thereby solvable at dc. The detailed explanation is given in Section III-C.

3) S-Parameter Extraction: Next we show how to combine u_o and u_i to obtain circuit parameters such as S-parameters of a circuit network. Shown in Fig. 6 is a p-port system. To extract S-parameters, both open- and short-circuit port conditions can be used. In the following, the open-circuit one is used for illustration.

With the open-circuit port condition, for a p-port system, we have p right-hand sides with the FEM system matrix $\mathbf{K}$ remaining unchanged. If we know V_i (the voltage at port i) and I_i (the current at port i) with $i = 1, 2, \ldots, p$ for each excitation (right-hand side), we can obtain S-parameters of the p-port network by solving

$$[V_i - Z_{\text{ref}} I_i] = \{S_{ij}\}_{p\times p}[V_j + Z_{\text{ref}} I_j], \quad i = 1, 2, \ldots, p; \quad j = 1, 2, \ldots, p \tag{22}$$

where Z_{ref} denotes the reference impedance (An industry standard Z_{ref} is 50 Ω). Since there are p excitations, there are p^2 rows of equations in (22), the solution of which is S_{ij}.

At high frequencies where the full-wave solution does not break down, the port voltage V_k $(k = 1, 2, \ldots, p)$ can be readily obtained from the $\mathbf{E}$ field outside conductors by evaluating a line integral from the port to the ground

$$V_k = \int_k u_o dl. \tag{23}$$

Assuming that the mth port is excited, the port current I_m is known from the excitation. At the other ports, I_k is zero since other ports are left open, i.e.,

$$I_k = 0, \qquad k = 1, 2, \ldots, m-1, m+1, \ldots, p. \tag{24}$$

At low frequencies, the voltage at each port, V_k, is obtained from u_o in the same way as (23), where u_o is the $\tilde{u_o}$ used in (19), which is $\text{Re}[u_{o,\text{ref}}]$. The current at each port, I_k, is the combination of the current flowing into the conductor at port k and that flowing through the dielectric region, i.e., through a capacitor. The current flowing into the conductor at port k, I_{kc}, can be evaluated from an area integral of u_i over the conductor cross section

$$I_{kc} = \int_k \sigma u_i dS. \tag{25}$$

Since we need to combine u_o and u_i to make a complete solution, the current that flows through the dielectric region at port k, I_{kd}, needs to also be incorporated. I_{kd} can be evaluated from

$$I_{kd} = j\omega C_k V_k \tag{26}$$

where C_k is the capacitance at port k. As a result, the total current I_k at port k is obtained from

$$I_k = I_{kc} + I_{kd}, \qquad k = 1, 2, \ldots, p. \tag{27}$$

There are two approaches to obtain the capacitance C_k $(k = 1, 2, \ldots, p)$ at each port. The first approach is to use the charge distributed at port k divided by V_k, where the charge can be obtained from normal $\mathbf{D}$ after (18) is solved.

The second approach that is more convenient to adopt in the proposed solution is to use the solution of u at the reference frequency ω_{ref} to extract C_k $(k = 1, 2, \ldots, p)$. We can do this because when the full-wave solution breaks down, the frequency is already low enough that the capacitance does not change with frequency any more. Hence, the capacitance extracted at the reference frequency can be safely used for lower frequencies. With u at ω_{ref} known, at the nonexcited ports, C_k can be found from

$$C_k = -I_{kc}/(j\omega_{\text{ref}} V_k). \tag{28}$$

At the excited port, C_k can be found from

$$C_k = (I_k - I_{kc})/(j\omega_{\text{ref}} V_k) \tag{29}$$

where I_k is the excitation current at port k at the reference frequency ω_{ref}, I_{kc} can be evaluated from u_i based on (25), and V_k is known from u_o.

As can be seen from the proposed procedure, the S-parameter extraction approach is the same at high and low frequencies. The only difference is that u (for voltage V_k) and current I_k $(k = 1, 2, \ldots, p)$ are generated differently. At high frequencies, u is solved directly from (17), and I_k $(k = 1, 2, \ldots, p)$ is analytically known. At low frequencies, u is solved by combining u_o and u_i, and I_k is obtained by combining the current flowing into the conducting region and that flowing into the dielectric region.

The overall procedure for the cases with conductor loss is summarized as follows.

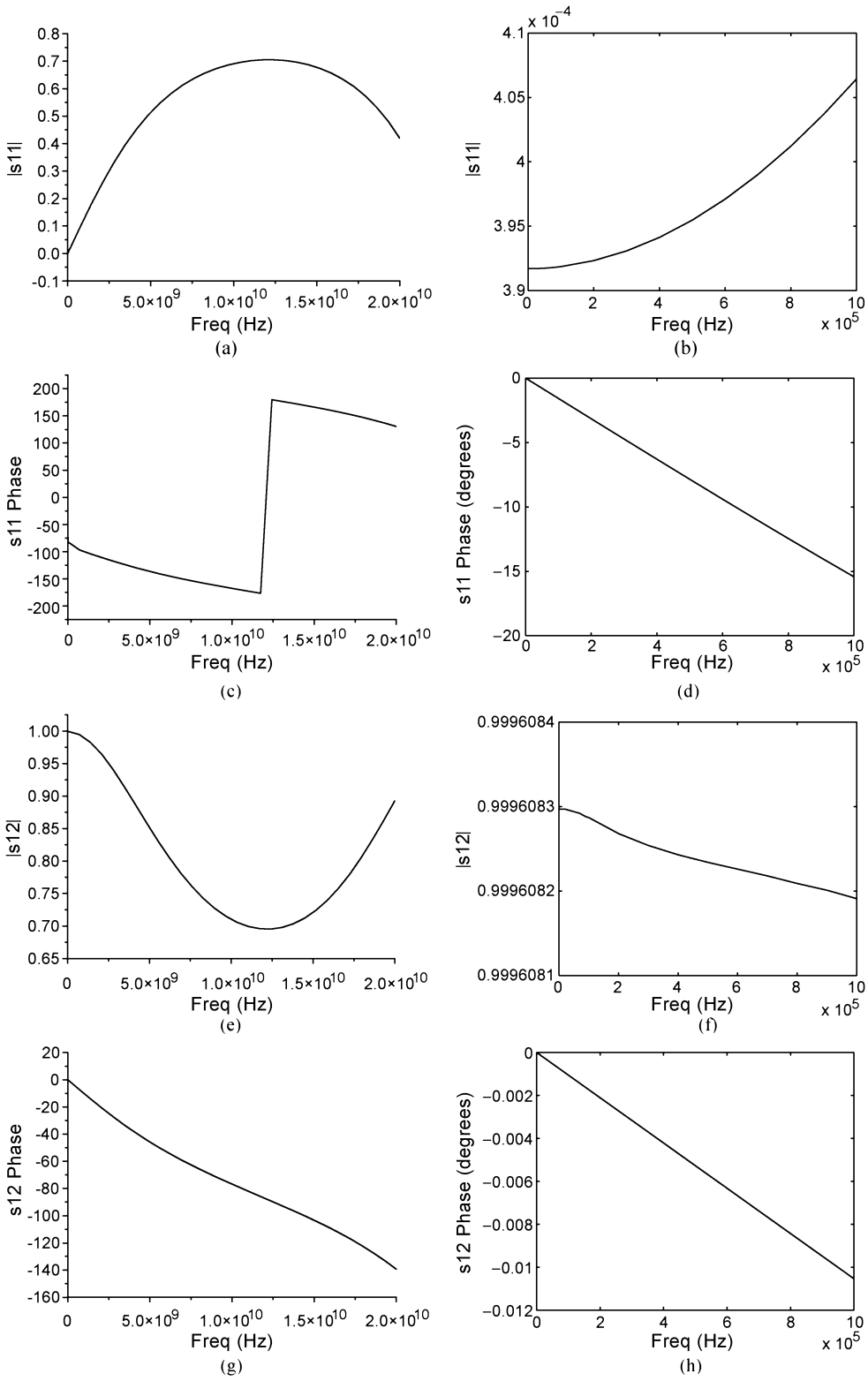

Fig. 10. S-parameters of a spiral inductor simulated by the proposed solution. (Left column: S-parameters in the entire band; right column: S-parameters at low frequencies.)

Step 1) When the full-wave solution breaks down, record u_{ref}, which is the field solution at the reference frequency. Use u_{ref} to derive the port capacitance C_k $(k = 1, 2, \ldots, p)$ using (28) and (29), where the voltage V_k and current I_{kc} are evaluated using (23) and (25), respectively.

Step 2) Use $\mathrm{Re}[u_{o,\mathrm{ref}}]$, the real part of the field solution outside conductors at the reference frequency, to evaluate the port voltage at port k, V_k, using (23).

Step 3) Use $\mathrm{Re}[u_{o,\mathrm{ref}}]$ as $\tilde{u}_o$ to solve (19). From the solution of (19), evaluate the current flowing into the conductor at port k by (25). Evaluate the current flowing through the dielectric region at port k by (26) using the port voltage obtained from Step 2) and the capacitance obtained from Step 1). Obtain the total current flowing into port k by (27).

Step 4) With the port voltage known from Step 2) and port current known from Step 3) at each frequency, extract S-parameters using (22).

The first two steps can be done once and reused for different low-frequency points since they are only related to u_{ref}. The last two steps are repeated for each frequency point. In other words, at low frequencies, we fix the voltage source excitation applied to the circuit, and extract the frequency-dependent current for each frequency.

C. DC Solution of $\mathbf{K}_{ii}$

At dc, $\mathbf{K}_{ii}$ becomes $\mathbf{S}_{ii}$. In general, the stiffness matrix $\mathbf{S}$ is only semipositive definite, and hence, has a null space. However, here, $\mathbf{S}_{ii}$ is formed not only by $\mathbf{S}$ inside conductors, but also by an additional matrix. This additional matrix is due to the contribution from the elements outside conductors, which share the same u_i unknowns with those elements inside conductors. Note that the unknowns residing on the conducting surface are shared by interior and exterior regions.

To help better understand the positive definiteness of the $\mathbf{S}_{ii}$, we use a 2-D discretization to illustrate the basic concept. Consider a 2-D mesh shown in Fig. 7. Element 1 represents an element in a conducting region, i.e., the u_i region. It is surrounded by the other three elements in the dielectric region, i.e., the u_o region. Using edge bases, a 3×3 $\mathbf{S}_{ii}$ matrix can be formed. It can be obtained as follows:

$$\mathbf{S}_{ii} = \mathbf{S} + \mathbf{Q} \tag{30}$$

where

$$\mathbf{S} = \frac{1}{\Delta_1}\begin{pmatrix} l_1 \\ l_2 \\ l_3 \end{pmatrix}(l_1 \quad l_2 \quad l_3)$$

and

$$\mathbf{Q} = \begin{pmatrix} \frac{l_1^2}{\Delta_4} & 0 & 0 \\ 0 & \frac{l_2^2}{\Delta_3} & 0 \\ 0 & 0 & \frac{l_3^2}{\Delta_2} \end{pmatrix} \tag{31}$$

where l_i denotes the length of the ith edge, and Δ_i denotes the area of the ith element. Given any arbitrary nontrivial vector x, the following properties of $\mathbf{S}$ and $\mathbf{Q}$ can be derived:

$$x^T\mathbf{S}x = \frac{1}{\Delta_1}(l_1x_1 + l_2x_2 + l_3x_3)^2 \geq 0 \tag{32}$$

$$x^T\mathbf{Q}x = \frac{l_1^2x_1^2}{\Delta_4} + \frac{l_2^2x_2^2}{\Delta_3} + \frac{l_3^2x_3^2}{\Delta_2} > 0. \tag{33}$$

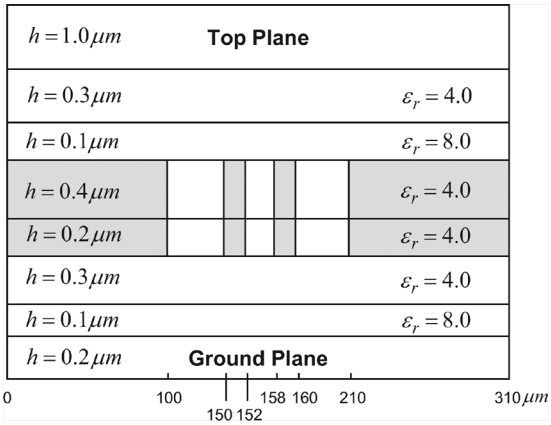

Fig. 11. Illustration of a 4×4 on-chip bus.

Clearly, since $x^T\mathbf{S}x$ is not always greater than zero, $\mathbf{S}$ is semipositive definite, and hence, cannot be inverted. However, $\mathbf{S}_{ii}$ is not made of $\mathbf{S}$ only. It has an additional $\mathbf{Q}$, which is contributed by the exterior elements, which share the edges on the conducting surface with interior elements. Since $\mathbf{Q}$ is positive definite, as shown in (33), the deficiency of $\mathbf{S}$ matrix is remedied. $\mathbf{S}_{ii}$ becomes well conditioned and solvable. In other words, after the null space of the original 3×3 $\mathbf{S}$ matrix is eliminated, it becomes a full-rank matrix. Therefore, in such cases, $\mathbf{S}_{ii}$ itself is an invertible matrix. $\mathbf{K}_{ii}$ is thus solvable even at dc. The above proof can also be applied to a 3-D discretization.

From the process of assembling $\mathbf{S}_{ii}$, it can be seen that regardless of 2-D or 3-D problems, the dimension of the matrix $\mathbf{Q}$ added upon the original stiffness matrix is equal to the number of edges on the conducting surface, i.e., the boundary between the interior and the exterior domains. At dc, there does not exist skin effect, and hence, current is uniformly distributed over the cross section that is perpendicular to the current flowing direction. Therefore, there is no need to add unknowns interior to conductors. Hence, the dimension of $\mathbf{S}_{ii}$ is the same as $\mathbf{Q}$. Since $\mathbf{Q}$ is positive definite, and $\mathbf{S}$ is semipositive definite, $\mathbf{S}_{ii}$ is also positive definite.

D. Identifying the Breakdown Frequency

To identify at which frequency the full-wave FEM-based solution breaks down, a natural solution is to execute the program from high to low frequencies. Once the circuit parameters extracted from the field solution, such as S-parameters, become physically meaningless, we consider the frequency as the breakdown frequency, at which the low-frequency solution is enabled. However, this procedure relies on physical intuition, which may not be accurate for complicated examples. For instance, consider an interconnect network connected by a lot of vias, given any port i of the network, generally, we expect that the diagonal entry of the S-parameter matrix, S_{ii}, is close to zero. However, S_{ii} may not be close to zero at all because of the large resistance of the network. Getting an S_{ii} that is equal to 0.6, for example, may not be wrong. We thus developed a rigorous analytical approach for quantitatively determining the breakdown frequency, which was reported in [14].

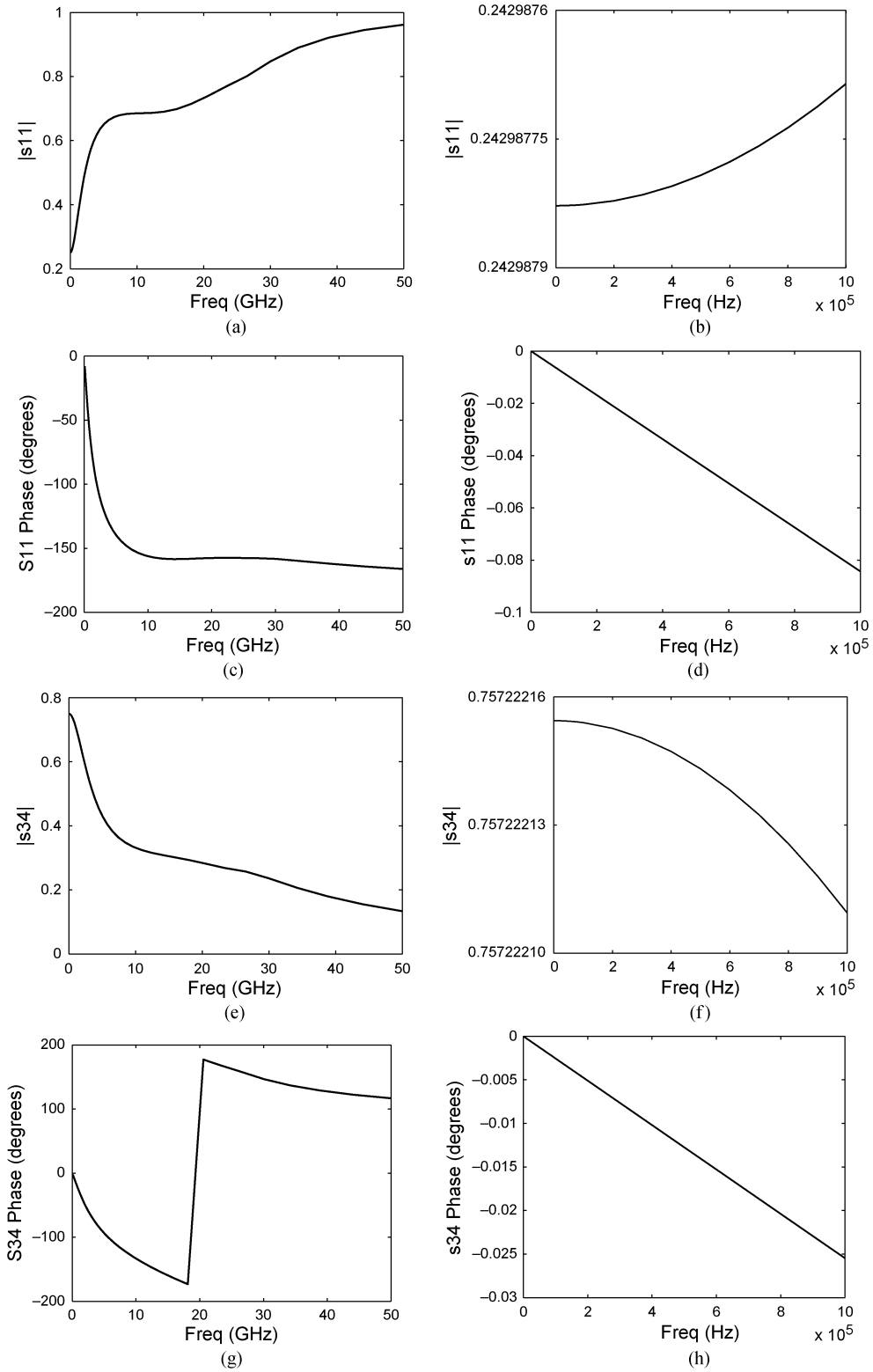

Fig. 12. S-parameters of a multiport structure simulated by the proposed solution. (Left column: S-parameters in the entire band; right column: S-parameters at low frequencies.)

IV. Numerical and Experimental Results

To validate the proposed solution, a number of on-chip interconnect and package inductor structures were simulated.

The first example was a three-metal-layer on-chip interconnect structure fabricated using silicon processing technology on a test chip [15]. The structure was of 300-μm width. It involved a 10-μm-wide strip in M2 layer, one ground plane in M1 layer, and one ground plane in M3 layer. The distance of this strip to

the M2 returns at the left- and right-hand sides was 50 μm. The strip was 2000-μm long. In [16], this structure was simulated successfully by a full-wave-based solver on which our low-frequency solution was built. The full-wave simulation broke down at 10 MHz, at which the low-frequency solution was enabled. The S-parameters of this structure were extracted, which are shown in Fig. 8. The figures in the left column depict the S-parameters in the entire frequency band in comparison with measured data, while those in the right column show the detail at low frequencies. As can be seen from the left column, the proposed solution agrees very well with the measured data from low frequencies to 50 GHz. Since the measured S-parameters were not available below 45 MHz, we compared the low-frequency result with that generated by a static solver, which was validated in [15]. As can be seen clearly from the right column of Fig. 8, the result generated by the proposed solution is in an excellent agreement with the reference data starting from dc. Thus, the accuracy of the proposed solution is validated. In addition, we extracted R and C parameters from the field solution. At dc, we obtained $R = 6.50455\ \Omega$ and $C = 4.45020$ pF, which showed an excellent agreement with analytical data.

With the proposed solution validated, we next simulated a 3-D spiral inductor residing on a package. The geometry of the spiral inductor is shown in Fig. 9. Its diameter (D) is 1000 μm. The wire is 100-μm wide, and 15-μm thick. The port separation (S) is 50 μm. The inductor is backed by two package planes. The backplane is 15-μm thick. The conductivity of the metal is 5.8×10^7 S/m. This structure was simulated successfully by the full-wave-based solver in [16] at high frequencies. The full-wave solution broke down around 1 MHz, at which the low-frequency solution was enabled. Fig. 10 shows the simulated S-parameters from dc to 20 GHz. Again, figures in the left column show the S-parameters over the entire frequency band, whereas those in the right column depict the detail at low frequencies. Based on the dc resistance of the inductor, the analytical S_{12} of the inductor is 0.999569151 at dc. The S_{12} generated by the proposed solution is 0.9996 at dc, which agrees very well with the analytical data.

To demonstrate the capability of the proposed solution in simulating multiport problems. In the third example, a four-port on-chip bus was simulated. Fig. 11 shows the detailed geometry and dielectric material information. The conductivity of the conductors is 5×10^7 S/m. Port 1 and port 2 are located at the near and far ends of the left wire, whereas the other two ports are located at the right wire. The FEM solution broke down around 10 MHz. With the proposed solution, we were able to successfully simulate the structure at frequencies as low as dc, as can be seen from Fig. 12. The analytical S_{11} and S_{34} are 0.25 and 0.75, respectively at dc. The simulated magnitude of S_{11} and S_{34} are 0.243 and 0.757, respectively. In addition, the phases of the simulated S_{11} and S_{34} are zero. Hence, both magnitude and phase produced by the proposed solution agree well with analytical data.

V. Conclusion

In this paper, we provided a theoretical analysis of the low-frequency breakdown problem observed in the 3-D full-wave FEM-based analysis of VLSI circuits. Based on this analysis, we develop an effective solution to completely remove the low-frequency breakdown problem. With this solution, we extend the capability of the full-wave FEM-based solver down to dc. In addition, across all the frequencies, the same system matrix is used in the proposed method, and hence, the method can be incorporated into any existing full-wave FEM-based CAD tool with minimal computational overhead. Moreover, from dc to frequency at which a typical full-wave solution breaks down, only the system matrix inside conductors has to be solved, and hence, the problem dimension is reduced greatly. The proposed method has been applied to the modeling of state-of-the-art VLSI circuits starting from dc. Numerical and experimental results have demonstrated its effectiveness in eliminating the low-frequency breakdown problem for full-wave FEM-based solutions.

Acknowledgment

The authors would like to thank Dr. M. J. Kobrinsky and Dr. S. Chakravarty, both with the Intel Corporation, Hillsboro, OR, for providing measured data.

References

[1] J. Zhao and W. C. Chew, "Integral equation solution of Maxwell's equations from zero frequency to microwave frequencies," *IEEE Trans. Antennas Propag.*, vol. 48, no. 10, pp. 1635–1645, Oct. 2000.

[2] A. Rong and A. C. Cangellaris, "Electromagnetic modeling of interconnects for mixed-signal integrated circuits from DC to multi-GHz frequencies," in *IEEE MTT-S Int. Microw. Symp. Dig.*, 2002, pp. 1893–1896.

[3] R. Dyczlj-Edllnger, G. Peng, and J. F. Lee, "Efficient finite element solvers for the Maxwell equations in the frequency domain," *Comput. Methods Appl. Mech. Eng.*, vol. 169, no. 3–4, pp. 297–309, Feb. 1999.

[4] S. C. Lee, J. F. Lee, and R. Lee, "Hierarchical vector finite elements for analyzing waveguiding structures," *IEEE Trans. Microw. Theory Tech.*, vol. 51, no. 8, pp. 1897–1905, Aug. 2003.

[5] S. Lee and J. Jin, "Application of the tree–cotree splitting for improving matrix conditioning in the full-wave finite-element analysis of high-speed circuits," *Microw. Opt. Technol. Lett.*, vol. 50, no. 6, pp. 1476–1481, Jun. 2008.

[6] S. Lee, K. Mao, and J. Jin, "A complete finite element analysis of multilayer anisotropic transmission lines from DC to terahertz frequencies," *IEEE Trans. Adv. Packag.*, vol. 31, no. 2, pp. 326–338, May 2008.

[7] Y. Chu and W. C. Chew, "A surface integral equation method for solving complicated electrically small structures," in *IEEE 14th Top. Elect. Perform. Electron. Packag. Meeting*, 2003, pp. 341–344.

[8] F. P. Andriulli, K. Cools, F. Olyslager, and E. Michielssen, "The Dottrick TDEFIE: A DC stable integral equation for analyzing transient scattering from PEC bodies," in *IEEE Int. AP-S Symp.*, July 2008, 4 pp.

[9] H. Bagci, F. P. Andriulli, F. Vipiana, G. Vecchi, and E. Michielssen, "A well-conditioned integral-equation formulation for transient analysis of low-frequency microelectronic devices," in *IEEE Int. AP-S Symp.*, Jul. 2008, 4 pp.

[10] J. Zhu and D. Jiao, "A unified finite-element solution from zero frequency to microwave frequencies for full-wave modeling of large-scale three-dimensional on-chip interconnect structures," *IEEE Trans. Adv. Packag.*, vol. 31, no. 4, pp. 873–881, Nov. 2008.

[11] J. M. Jin, *The Finite Element Method in Electromagnetics*. New York: Wiley, 2002.

[12] D. Ruiz, "A scaling algorithm to equilibrate both row and column norms in matrices," Rutherford Appleton Lab., Oxon, U.K., Tech. Rep. RAL-TR-2001-034, 2001, also appeared as ENSEEIHT-IRIT Re. RT/APO/01/4.

[13] J. B. Manges and Z. J. Cendes, "A generalized tree-cotree gauge for magnetic field computation," *IEEE Trans. Magn.*, vol. 31, no. 3, pp. 1342–1347, May 1995.

[14] J. Zhu and D. Jiao, "A theoretically rigorous full-wave finite-element-based solution of Maxwell's equations from DC to high frequencies," *IEEE Trans. Adv. Packag.*, 2010, to be published.

[15] M. J. Kobrinsky, S. Chakravarty, D. Jiao, M. C. Harmes, S. List, and M. Mazumder, "Experimental validation of crosstalk simulations for on-chip interconnects using S-parameters," *IEEE Trans. Adv. Packag.*, vol. 28, no. 1, pp. 57–62, Feb. 2005.
[16] D. Jiao, S. Chakravarty, and C. Dai, "A layered finite-element method for high-capacity electromagnetic analysis of high-frequency ICs," *IEEE Trans. Antennas Propag.*, vol. 55, no. 2, pp. 422–432, Feb. 2007.
[17] A. Alonso Rodriguez and A. Valli, "Voltage and current excitation for time–harmonic eddy current problems," *SIAM J. Appl. Math.*, vol. 68, pp. 1477–1494, 2008.

Jianfang Zhu (S'09) received the B.S. degree in electronic engineering and information science from the University of Science and Technology of China, Hefei, China, in 2006, and is currently working toward the Ph.D. degree at Purdue University, West Lafayette, IN.

She is currently with the On-Chip Electromagnetics Group, Purdue University, as a Research Assistant. Her current research interest is computational electromagnetics for large-scale high-frequency IC design.

Dan Jiao (S'00–M'02–SM'06) received the Ph.D. degree in electrical engineering from the University of Illinois at Urbana-Champaign, in 2001.

She then joined the Technology Computer-Aided Design (CAD) Division, Intel Corporation, until September 2005, as a Senior CAD Engineer, Staff Engineer, and Senior Staff Engineer. In September 2005, she joined Purdue University, West Lafayette, IN, as an Assistant Professor with the School of Electrical and Computer Engineering. In 2009, she became a tenured Associate Professor. She has authored two book chapters and over 100 papers in refereed journals and international conferences. Her current research interests include computational electromagnetics, high-frequency digital, analog, mixed-signal, and RF IC design and analysis, high-performance very large scale integration (VLSI) CAD, modeling of microscale and nanoscale circuits, applied electromagnetics, fast and high-capacity numerical methods, fast time-domain analysis, scattering and antenna analysis, RF, microwave, and millimeter-wave circuits, wireless communication, and bio-electromagnetics.

Dr. Jiao has been a reviewer for many IEEE journals and conferences. She is an associate editor for the IEEE TRANSACTIONS ON ADVANCED PACKAGING. She was the recipient of the 2010 Ruth and Joel Spira Outstanding Teaching Award, the 2008 National Science Foundation (NSF) CAREER Award, the 2006 Jack and Cathie Kozik Faculty Start up Award (which recognizes an outstanding new faculty member of the School of Electrical and Computer Engineering, Purdue University), a 2006 Office of Naval Research (ONR) Award under the Young Investigator Program, the 2004 Best Paper Award presented at the Intel Corporation's annual corporate-wide technology conference (Design and Test Technology Conference) for her work on generic broadband model of high-speed circuits, the 2003 Intel Corporation Logic Technology Development (LTD) Divisional Achievement Award in recognition of her work on the industry-leading BroadSpice modeling/simulation capability for designing high-speed microprocessors, packages, and circuit boards, the Intel Corporation Technology CAD Divisional Achievement Award for the development of innovative full-wave solvers for high-frequency IC design, the 2002 Intel Corporation Components Research the Intel Hero Award (Intel-wide she was the tenth recipient) for timely and accurate 2-D and 3-D full-wave simulations, the Intel Corporation LTD Team Quality Award for her outstanding contribution to the development of measurement capability and simulation tools for high-frequency on-chip crosstalk, and the 2000 Raj Mittra Outstanding Research Award presented by the University of Illinois at Urbana-Champaign.